June 21, 2022 Volume 38, Number 24 pubs.acs.org/Langmuir

LANGMUIR

The ACS journal of fundamental interface science

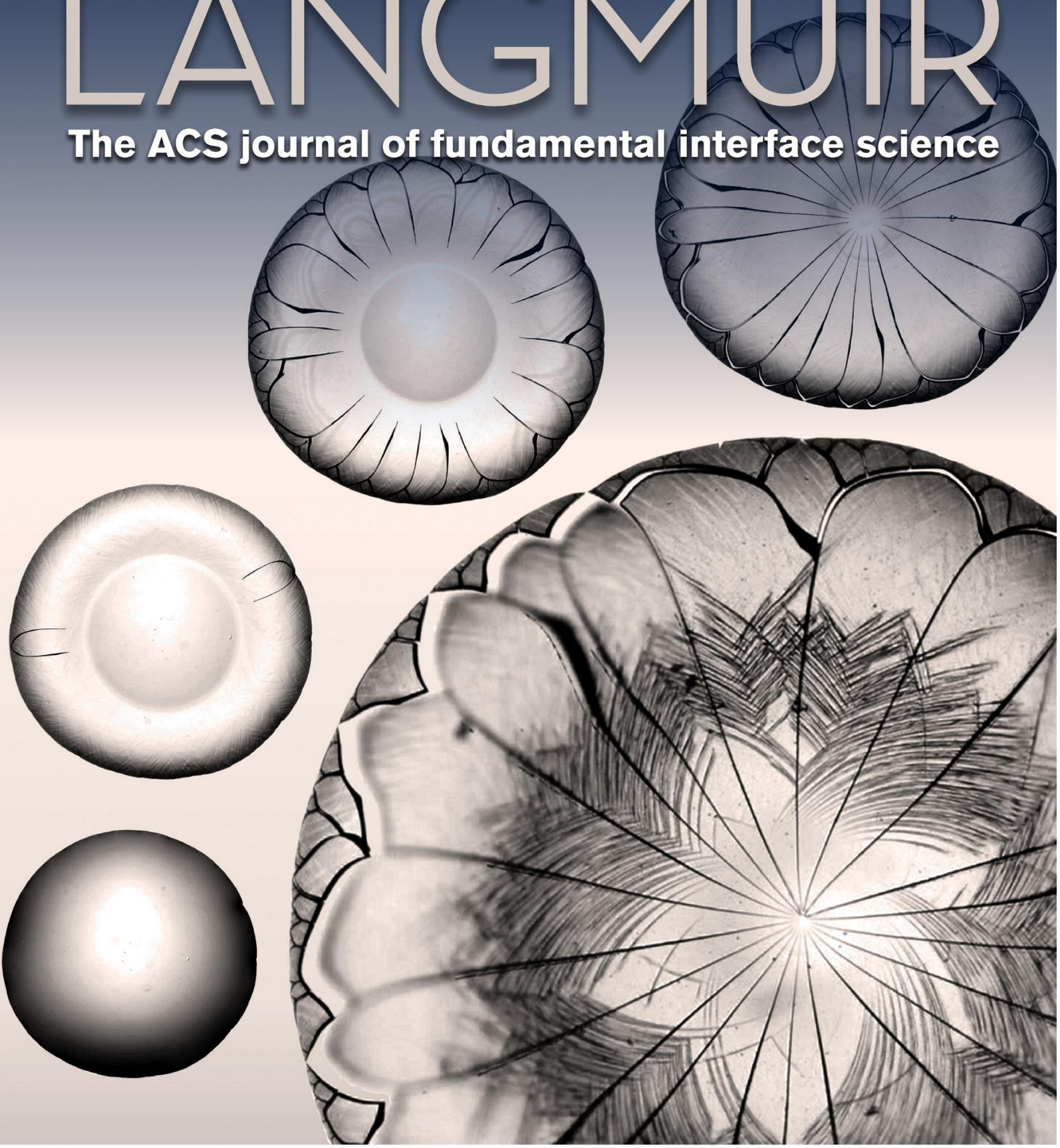

ACS Publications
Most Trusted. Most Cited. Most Read.

www.acs.org

LANGMUIR

pubs.acs.org/Langmuir Article

Criteria for Crack Formation and Air Invasion in Drying Colloidal Suspensions

Paul Lilin* and Irmgard Bischofberger*

Cite This: *Langmuir* 2022, 38, 7442−7447 Read Online

ACCESS | Metrics & More | Article Recommendations | Supporting Information

ABSTRACT: The drying of sessile drops of aqueous colloidal suspensions leads to the formation of a close-packed particle deposit. As water evaporates, a solidification front propagates from the edge of the drop toward the center, leaving behind a thin disk-shaped deposit. For drops with sufficiently large particle volume fractions, the deposit eventually covers the entire wetted area. In this regime, the dynamics of the deposit growth is governed by volume conservation across a large range of particle volume fractions and drying times. During drying, water flows radially through the deposit to compensate for evaporation over the solid's surface, creating a negative pore pressure in the deposit which we rationalize with a hydrodynamic model. We show that the pressure inside the deposit controls both the onset of crack formation and the onset of air invasion. Two distinct regimes of air invasion occur, which we can account for using the same model that further provides a quantitative criterion for the crossover between the two regimes.

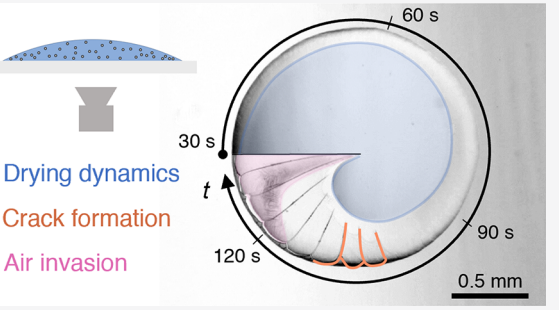

INTRODUCTION

Cracked paint on building facades, fractured mud in dry regions, and desiccation cracks in drops of blood illustrate the fragility of films composed of colloidal suspensions.[1−4] As the solvent evaporates from a suspension placed on a substrate, a solid deposit of close-packed particles is left behind.[5−8] This deposit fractures into a variety of patterns depending on its thickness and the solvent, particle, substrate, and air properties.[9−20] Controlling or preventing this thin film failure requires a thorough understanding of the microscale mechanics and flows, from the initial deposition to the evaporation of the last water molecule.

When a drop of a colloidal suspension is deposited on a hydrophilic substrate, its contact line remains pinned to the substrate.[21] Particles are brought to the drop edge by enhanced evaporation at the contact line and a capillary-driven flow, which leads to the formation of the close-packed solid particle deposit.[6,22] For drops with an initial particle volume fraction of $\phi_0 \gtrsim 0.08$, the solid deposit grows inward and eventually covers almost the entire initially wetted area.[9,12,17,23−26] The solid deposit is saturated with water, and its growth is driven by evaporation occurring on its top, which brings solvent and particles from the liquid region in the center of the drop to the solid deposit.[25,27] For suspensions of hard particles, two key events occur during drying: radial cracks propagate from the drop edge toward the center, and, at a later time, air invades the deposit.[9,12,25,28] The critical stress acting on the deposit beyond which cracks form has been determined by applying a homogeneous pressure to the deposit[29] and by measuring the bending of a thin cantilever covered by a colloidal suspension film.[30,31] These techniques, however, do not capture the critical role of the solidification front for the stress distribution.[25,32] The dynamics of air invasion have been characterized at the pore scale but are rarely measured for the entire drop.[17,33]

In this article, we show that both the onset of crack formation and the onset of air invasion can be rationalized by considering the pore pressure in the deposit, which we calculate using a hydrodynamic model. Tensile stresses associated with the pore pressure are released through the formation of a crack at a critical value set by a linear elastic Griffith criterion, while the threshold for air invasion is governed by the maximum attainable curvature of the microscopic menisci between the particles. Our hydrodynamic model explains the strong dependence of the onset of crack formation and air invasion on drying conditions. The deposit growth, in contrast, exhibits a universal dynamics set by volume conservation. This understanding of the pressure distribution and how it changes once the liquid region in the center of the drop dries out completely explains the two distinct dynamics we observe for the invasion of air into the deposit.

EXPERIMENTAL METHODS

Drop drying experiments are performed using charge-stabilized suspensions of colloidal silica particles (Ludox AS-40, Sigma-Aldrich)

Received: February 16, 2022
Revised: April 28, 2022
Published: May 23, 2022

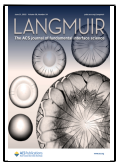

https://doi.org/10.1021/acs.langmuir.2c00397
Langmuir 2022, 38, 7442−7447

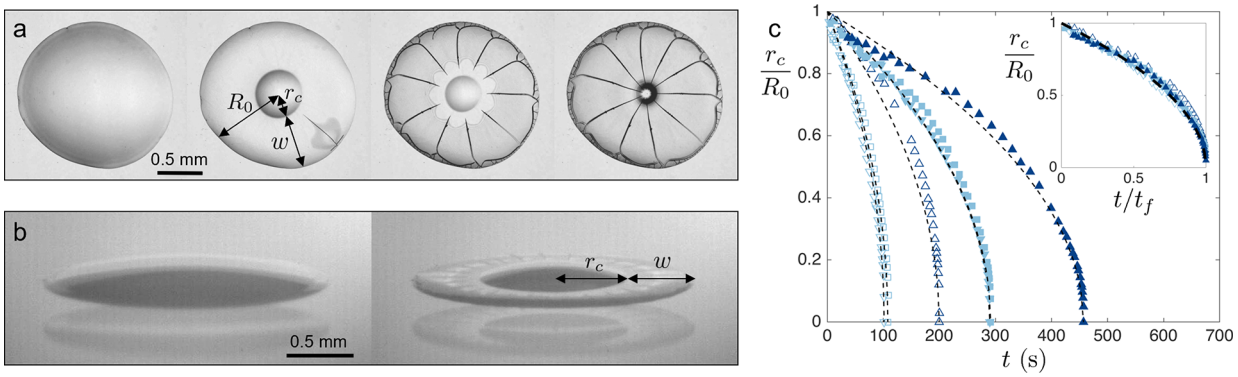

Figure 1. Drying of a colloidal suspension drop. (a) Bottom view of a drop of a silica particle suspension with deposition radius R_0 = 850 μm (initial drop volume Ω_0 = 0.3 μL) and initial particle volume fraction ϕ_0 = 0.23 drying on a glass slide at a relative humidity of RH = 27%. A solid deposit forms at the edge of the drop and grows as the liquid spherical cap of radius r_c in the center recedes. When the deposit width w reaches a critical value, the first radial crack forms in the deposit, followed by regularly spaced radial cracks. At time $t = t_f$, the liquid cap completely dries out and the cracks reach the center. (b) Side view of a drop with R_0 = 1050 μm and ϕ_0 = 0.18 drying at a relative humidity of RH = 22%. (c) The temporal evolution of the liquid cap retraction is well described by a volume-conservation-based model (dashed lines). Legend: ▽, Ω_0 = 0.3 μL, ϕ_0 = 0.16, RH = 21%; □, Ω_0 = 0.3 μL, ϕ_0 = 0.12, RH = 27%; △, Ω_0 = 0.3 μL, ϕ_0 = 0.16, RH = 50%; ▼, Ω_0 = 1 μL, ϕ_0 = 0.16, RH = 21%; ■, Ω_0 = 1 μL, ϕ_0 = 0.12, RH = 21%; and ▲, Ω_0 = 1 μL, ϕ_0 = 0.16, RH = 51%.

of diameter $2a$ = 22 nm. The suspensions are diluted with deionized water to particle volume fractions of ϕ_0 = 0.08−0.23. The diluted suspensions are stable. Drops of volume Ω_0 = 0.3−1 μL are deposited on clean microscope glass slides using a micropipette (Gilson 0.2−2 μL), where they adopt a contact angle of 20 ± 2°. Prior to use, the glass slides are cleaned by sonication in acetone for 5 min, followed by rinsing with isopropanol, and the colloidal suspensions are sonicated for 20 min to ensure a complete dispersion. The drops are placed in a transparent box to suppress air flow, at ambient temperature T = 22 ± 2 °C and a constant relative humidity (RH) ranging from 7 to 70%. We image the drops from below using an inverted microscope (Eclipse TE2000-U, Nikon with Lumix GH5 camera) with magnification 6×, filmed at 30 fps.

RESULTS AND DISCUSSION

The drops adopt a spherical cap shape of radius R_0, as shown in Figure 1a,b. As water evaporates, the initial contact line remains pinned. A close-packed particle deposit of width w forms from the drop edge, enclosing a liquid spherical cap of radius r_c that shrinks as the solidification front moves inward.[24,25] At a deposit width of w_{crack}, the first radial crack appears in the deposit, rapidly followed by a succession of regularly spaced radial cracks which propagate toward the center of the drop as the liquid cap recedes (Video S1).[9,12] At time t_f, the liquid cap dries out, r_c = 0, and the deposit covers the entire initial drop area, $w = R_0$. The disk-shaped deposit has a nearly constant thickness of h, as shown in Figure S1.

We monitor the dynamics of the liquid cap retraction for drops of varying initial volumes and particle volume fractions drying at different relative humidities (RH), as displayed in Figure 1c. The deposit formation and retraction of the liquid cap are slow at early times and gradually accelerate until the liquid cap rapidly vanishes as $t \to t_f$. Larger initial drop volumes and higher RH increase the total drying time t_f. At fixed initial drop volume and RH, lowering the initial particle volume fraction slightly increases t_f. Remarkably, normalizing the time t with the total drying time t_f leads to a master curve of all of the data, as shown in the inset of Figure 1c; all drops exhibit universal deposit growth dynamics as represented visually in Figure S2.

To rationalize the universal dynamics, we consider the volume conservation between the deposit of volume $\Omega_{deposit}$ and the liquid spherical cap of volume Ω_{cap}, which both contain water and particles. As the drop dries, its volume decreases at an evaporation rate $\dot{\Omega}$ that remains constant during deposit formation, as shown by mass measurements (Figure S3) and in agreement with previous findings.[27,34] The total volume of the drop at a time t after deposition is then $\Omega_{cap} + \Omega_{deposit} = \Omega_0 - \dot{\Omega}t$, where Ω_0 is the initial drop volume. The volume of particles remains constant and equal to $\Omega_0\phi_0 = \Omega_{cap}\phi_{cap} + \Omega_{deposit}\phi_{deposit}$, where ϕ_0 is the initial particle volume fraction, ϕ_{cap} is the particle volume fraction in the liquid cap, and $\phi_{deposit}$ is the particle packing fraction in the deposit. At the end of the drying, Ω_{cap} = 0, from which we obtain an expression for the drying time t_f that depends on the initial particle volume fraction and the evaporation rate, assuming no air invades the deposit:

$$t_f = \frac{\Omega_0}{\dot{\Omega}}\left(1 - \frac{\phi_{deposit}}{\phi_0}\right) \quad (1)$$

To obtain an analytical expression for the deposit growth, we assume a constant deposit thickness h and a constant particle volume fraction in the liquid cap, $\phi_{cap} \approx \phi_0$. The volume conservation then simplifies to

$$\frac{r_c}{R_0} = \sqrt{1 - \frac{t}{t_f}} \quad (2)$$

where r_c is the liquid cap radius and R_0 is the initial radius of the deposited drop. Equation 2 captures the deposit formation remarkably well despite the simplicity of our assumptions, as seen in Figure 1c. We note that the liquid cap volume fraction ϕ_{cap} is difficult to measure and could be affected by the flows of water and particles from the liquid cap to the deposit and by water evaporation from the liquid cap that would increase ϕ_{cap}. Indeed, hydrodynamic simulations show that ϕ_{cap} increases during drying.[24] Such an increase would slow down the deposit formation at early times, as particles would remain in the liquid cap instead of residing in the deposit. Our data shows some evidence of an increase in ϕ_{cap}; we observe a slight deviation to higher values of r_c/R_0 compared to the prediction from eq 2 that assumes $\phi_{cap} = \phi_0$. More importantly though, our results demonstrate that the deposit formation dynamics is first and foremost governed by volume conservation, while changes in ϕ_{cap} have a much smaller influence.

https://doi.org/10.1021/acs.langmuir.2c00397
Langmuir 2022, 38, 7442−7447

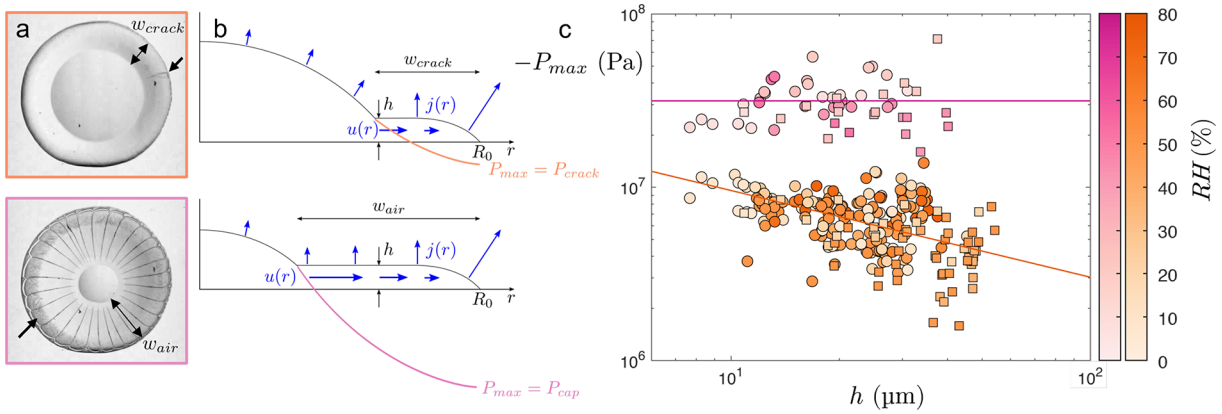

Figure 2. Pressure in the deposit determines the onset of crack formation and the onset of air invasion. (a) Bottom views of a 0.3 μL suspension drop with $\phi_0 = 0.08$ drying at RH = 10%, at the moment when the first crack appears (top) and when air invasion becomes visible (bottom). The arrows denote the first crack (top) and the dark air invasion front located toward the edge of the deposit (bottom). (b) Schematics of the drop at these two instants in time. $u(r)$ denotes the radial flow velocity through the porous deposit, $j(r)$ is the evaporative flux, and h is the deposit thickness. The colored lines represent the pressure profiles $P(r)$ in the deposit. (c) Maximally negative pressures $P_{max} = P(R_0)$ in the deposit at the onset of cracking (bottom, orange) and at the onset of air invasion (top, purple) versus the deposit thickness h. Symbols indicate the initial drop volume: ●, $\Omega_0 = 0.3$ μL; ■, $\Omega_0 = 1$ μL. The color shades indicate the relative humidity. The orange line denotes $P_{max} = -(1-\nu)/(1-2\nu)\sqrt{G_c E/h}$, with $\nu = 0.3$ and $\sqrt{G_c E} = 1.7 \times 10^4$ Pa m$^{1/2}$. The purple line denotes $P_{max} = -4.8\gamma/a$.

Two key events occur in the "life" of a drying drop. The first event is the appearance of a first crack in the deposit,[12,13,35] which occurs at a deposit width of w_{crack} (Figure 2a). This crack is quickly followed by a series of regular radial cracks that form with avalanche-like dynamics mediated by the delamination of the deposit from the substrate.[9,10,12] As the deposit grows, the cracks propagate inward with a stop-and-go motion while maintaining a thin crack-free ring of deposit close to the liquid cap.[25,36,37] The second event is the invasion of the deposit by air,[17,25,33] which occurs at a deposit width of w_{air}. As air progressively replaces the water inside the deposit, the deposit becomes opaque,[17] as seen in Figure 2a. What determines the onsets of crack formation and air invasion?

Water evaporates from the deposit as the drop dries, and this lost volume must be replaced either by air or by water from the liquid cap. The surface of the deposit consists of microscopic water−air menisci pinned between the particles. The energy cost of creating a new interfacial area upon air invasion is higher than the energy required for water to flow from the liquid cap into the deposit and radially through the deposit.[5,25] As a result, the deposit remains saturated with water.[23] Because of volume conservation and the thin nature of the deposit ($h \ll R_0$), the radial flow velocity through the deposit induced by the evaporation at the deposit surface is much greater than the vertical flow velocity.[27] This in-plane flow generates a viscous pore pressure drop in the deposit. The resulting pore pressure $P(r)$ inside the deposit is balanced with atmospheric pressure at the microscopic water−air meniscus *via* the capillary pressure $P_{atm} - P(r) \sim \gamma\kappa(r)$, where γ is the water surface tension and $\kappa(r)$ is the curvature of the meniscus. As the deposit continues to grow, the pressure drop increases, which ultimately leads to crack formation and air invasion.[11,17,25,27] To establish quantitative criteria for the onsets of cracking and air invasion, we need a model that describes the pore pressure in the deposit at these critical moments.

Evaporation is the driving process for the formation of cracks, and it is thus the starting point of the model. For a drop with the shape of a thin disk, the local evaporative flux $j(r)$ is set by water vapor diffusion in the air surrounding the drop and varies spatially as $j(r) = j_0/2(1 - (r/R_0)^2)^{-1/2}$,[38,39] as sketched in Figure 2b, where $j_0 = \dot{\Omega}/(\pi R_0^2)$. Advection due to air flows can make the evaporative flux uniform instead of divergent at the boundary of the drop,[39] but we find that considering the divergent evaporative flux leads to a better agreement with the data, as shown in Figure S4. To compensate for the evaporative flux of water out of the deposit, volume conservation requires a radial flow of water through the porous deposit that satisfies $h\partial(ur)/\partial r + rj = 0$, which yields a radial flow velocity of $u(r) = j_0 R_0/(2h)\sqrt{R_0^2 - r^2}/r$. To overcome viscous dissipation, this flow requires a pressure gradient obtained from Darcy's law as $\partial P/\partial r = -\mu/k u(r)$, where $P(r)$ is the liquid pressure inside the pores, μ is the dynamic viscosity of water, and k is the deposit permeability estimated using the Kozeny−Carman equation $k = \frac{1}{45}\frac{(1-\phi_{deposit})^3}{\phi_{deposit}^2}a^2$ with a being the particle radius and $\phi_{deposit} \approx 0.6$.[29,40,41] Combining Darcy's law with volume conservation yields the pore pressure profile $P(r)$, shown in Figure S5. Note that because $h \ll R_0$, we consider the pressure to be uniform in the vertical direction. As the flow in the deposit is radially outward, the pressure monotonically decreases with r and reaches a maximally negative pressure of $P_{max} = P(R_0)$ at R_0. Integrating $\partial P/\partial r$ across the deposit radius yields

$$P_{max} = P(r_c) - \frac{\mu j_0 R_0^2}{2kh}\left(\operatorname{arctanh}\sqrt{1-\left(\frac{r_c}{R_0}\right)^2} - \sqrt{1-\left(\frac{r_c}{R_0}\right)^2}\right) \quad (3)$$

This expression contains the porous pressure scale $P^* = (\mu j_0 R_0^2)/(kh)$ associated with flow in the thin deposit,[42] multiplied by a factor that increases with the deposit width $w = R_0 - r_c$ over which water evaporates. The liquid pressure at r_c, $P(r_c)$, can be evaluated as the sum of three terms that are all much smaller than P^* for small particles ($k \ll h^2$): the atmospheric pressure, the pressure contribution from the liquid cap curvature γ/r_c, and the pressure contribution from viscous flow inside the liquid cap $\mu_{susp} j_0 R_0^2/h^3$, with μ_{susp} being the

https://doi.org/10.1021/acs.langmuir.2c00397
Langmuir 2022, 38, 7442−7447

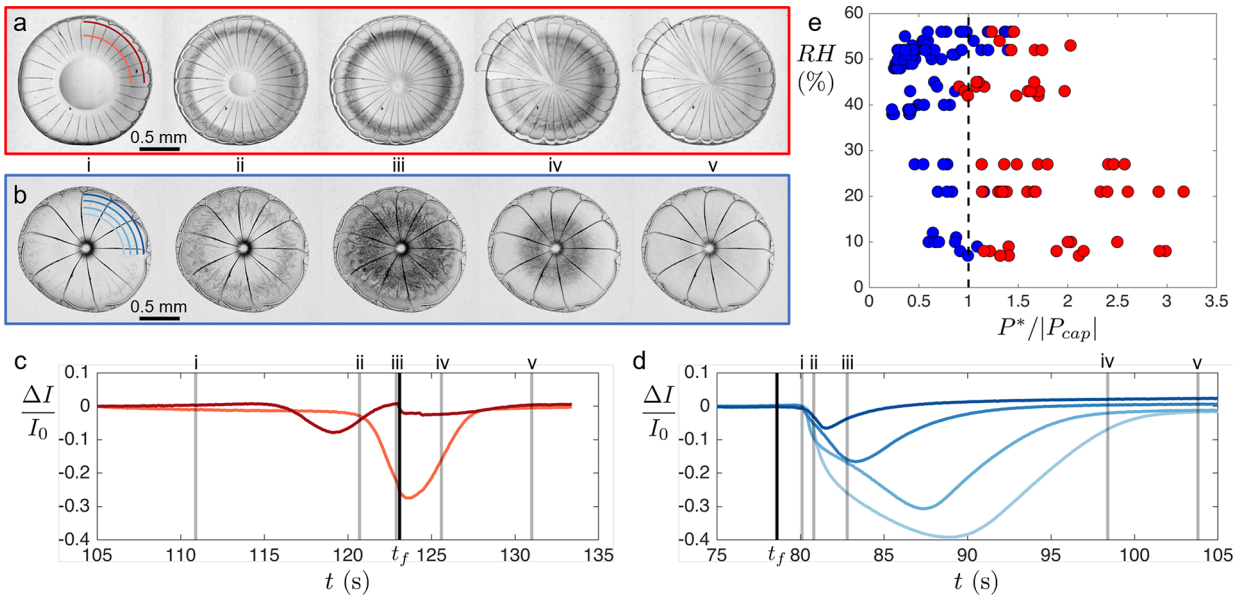

Figure 3. Air invasion occurs in two distinct ways. (a) Air invasion occurring while the liquid cap is still retracting appears as a bandlike dark front. The front moves from the edge to the center of the drop. (b) Air invasion occurring after the liquid cap has dried out appears as a diffuse dark region covering the entire deposit. (c) Temporal evolution of the change in transmitted light intensity ΔI, normalized by the background intensity outside the drop I_0, for the bandlike air invasion regime. ΔI is measured in the 20-μm-wide regions highlighted in (a) at $r/R_0 = 0.7$ and 0.9. The gray lines correspond to images (i–v) in (a), and the black line denotes the time when the liquid cap completely dries out, $t = t_f$. The intensity starts to decrease for $t < t_f$, and the front passes through the $r/R_0 = 0.9$ region before reaching the $r/R_0 = 0.7$ region. (d) $\Delta I/I_0$ for the diffuse air invasion regime, measured in the 20-μm-wide regions highlighted in (b) at $r/R_0 = 0.6$, 0.7, 0.8, and 0.9. The intensity decreases for $t > t_f$ and starts to decrease at the same time in all four regions. (e) State diagram denoting the regions of bandlike (red) and diffuse (blue) air invasion for different values of RH. The transition between the two regimes occurs at $|P_{cap}| \approx P^*$.

dynamic viscosity of the suspension in the liquid cap.[24] We neglect $P(r_c)$ in the following.

The negative pressure in the deposit is a result of the water–air menisci at the top surface of the deposit. As the menisci are pinned to the surrounding particles, water lost to evaporation is replaced by water molecules underneath, which generates a tension force resulting in a negative pressure.[43] The capillary forces acting on the menisci have a vertical component, which induces stresses in the solid deposit.[25,44] This vertical component, combined with the adhesion of the deposit to the substrate that prevents radial expansion, leads to a state of tensile stress $\sigma_{rr} = -(1-2\nu)/(1-\nu)P$, where ν is the Poisson ratio of the porous deposit.[45] As the deposit width w increases, the pore pressure at R_0 becomes increasingly negative, and the tensile stresses are relaxed by the formation of a crack at $w = w_{crack}$.

At which critical stress does the deposit fail? We express the deposit thickness h from the volume conservation of the particles $\phi_0\Omega_0 = \phi_{deposit}\pi {R_0}^2 h$ and the mean evaporative flux $j_0 = \dot{\Omega}/(\pi {R_0}^2)$, where $\dot{\Omega}$ is evaluated using eq 1, and we measure the deposit width w_{crack} at crack formation to obtain the pore pressure in the deposit at cracking $P_{max}(w_{crack})$ from eq 3. The pore pressure scales linearly with the tensile stress in the deposit with a constant prefactor of $(1-2\nu)/(1-\nu)$ that is close to unity.

Neither the drop size R_0 nor the mean evaporative flux j_0 exhibit a systematic effect on $P_{max}(w_{crack})$ as shown in Figure 2c, where we report drops of different volumes and at various relative humidities. An increase in deposit thickness, however, causes a systematic decrease in the pressure necessary to form a crack, $P_{max}(w_{crack})$, and thus the tensile stress at crack formation exhibits a power-law dependence with the deposit thickness with an exponent of -0.4 ± 0.1. Measurements that directly impose a pressure on the deposit in an ultrafiltration cell (instead of letting it dry) found a similar power law with exponent -0.4 for the pressure at crack formation.[29] We can rationalize this dependence by considering the Griffith criterion for thin sheets that balances the elastic energy released by forming a crack of length L, which scales as $\sigma\varepsilon h^2 L$ where ε is the strain, and the cost $G_c hL$ of creating the crack.[41] The critical energy release rate G_c accounts for the surface energy cost associated with creating crack surfaces and for the energy cost associated with plastic rearrangements of the particles.[45,46] For an elastic material with Young's modulus E, $\sigma = E\varepsilon$, and the stress at crack formation then scales as $h^{-1/2}$, in fair agreement with our data. Moreover, a fit of $P(w_{crack}) = -(1-\nu)/(1-2\nu)\sqrt{G_c E/h}$ yields a fracture toughness $K_c = \sqrt{G_c E} = 1.7 \times 10^4$ Pa m$^{1/2}$, which is comparable to the value of $K_c = 9.9 \times 10^4$ Pa m$^{1/2}$ reported in the literature.[46] We note that nonlinear stress–strain relations proposed for deposits of hard spherical particles predict the stress at crack formation to scale as $h^{-2/3}$[30,41] or $h^{-3/5}$,[29,47] in lesser agreement with our experimental findings than the model assuming a linear elastic material.

Although the stresses are relaxed by crack formation,[32] the pore pressure in the deposit does not change significantly after the formation of cracks given that it is set by radial flows in the deposit. The pressure at the outer edge of the deposit becomes increasingly negative as the deposit grows. Eventually, at a deposit width w_{air}, a dark front appears in the deposit (Figure 2a). The front identifies the region of the deposit where air has partially replaced water, which induces refractive index fluctuations that decrease the transmitted light intensity; the deposit is transparent when it is saturated with either water or air alone.[17] We calculate the pore pressure at which air invasion occurs, $P_{max}(w_{air})$, using eq 3. $P_{max}(w_{air})$ is a constant value independent of drop size, evaporation rate, or deposit thickness,

https://doi.org/10.1021/acs.langmuir.2c00397
Langmuir 2022, 38, 7442–7447

as shown in Figure 2c. For the pore pressure to remain balanced against atmospheric pressure as the deposit grows, the curvature κ of the microscopic water−air menisci at the top of the deposit needs to become progressively smaller. However, the curvature is bound by the pore size, leading to a maximum attainable capillary pressure calculated from the specific surface area of the nanoparticles as $P_{cap} = -6.1\gamma/a$.[48] When the pore pressure becomes lower than P_{cap}, the energy required to pull water from the liquid cap through the porous deposit becomes larger than the increase in surface energy caused by displacing the water−air interface. Consequently, the menisci recede inside the layers of particles and air invades the deposit.[33] We find $P_{max}(w_{air}) = -(4.8 \pm 0.4)\gamma/a$, confirming the accuracy of our model.

Remarkably, air invasion can occur in two ways: (i) The black front appears as a sharp band while the liquid cap is still receding ($w_{air} < R_0$) and moves toward the center of the drop, as seen in Figure 3a and Video S1. The propagation of the band is captured in Figure 3c, where we report the change in transmitted light intensity ΔI normalized by the background intensity I_0 in two regions at radii of $r/R_0 = 0.7$ and 0.9. The advancing dark band identifies the region where the pore pressure in the deposit has reached the capillary pressure P_{cap}. (ii) Air invasion occurs only after the liquid cap has dried out ($w_{air} = R_0$), as shown in Figure 3b and Video S2. The dark air-invaded region is diffuse and rapidly covers the entire deposit, as evidenced by the transmitted light intensity that decreases simultaneously in four regions at different radii $r/R_0 = 0.6-0.9$, as shown in Figure 3d. The diffuse propagation denotes the transition from horizontal drying to vertical drying. With the liquid cap gone, the water now flows predominantly in the vertical direction because the evaporation from the top of the deposit governs the flow direction.

The mode of air invasion depends on the value of the porous pressure scale, $P^* = \mu j_0 {R_0}^2/(kh)$, with respect to the capillary pressure P_{cap}. For drops with $P^* > |P_{cap}|$, air invasion occurs as a dark band; for drops with $P^* < |P_{cap}|$, the air invades as a delayed diffuse front, as displayed in Figure 3e. The change in transmitted light intensity caused by air invasion thus provides a striking visualization of the pressure distribution in the deposit during the later stages of drying.

CONCLUSIONS

Our comprehensive investigation of the drying dynamics of colloidal suspension drops provides quantitative criteria for the two key events occurring during drying: crack formation and air invasion. Considering the flow-induced pressure distribution in the porous deposit, we show that the onset of cracking is set by a linear elastic Griffith criterion whereas the onset of air invasion is set by the maximum capillary pressure at the menisci between particles. The delicate balance between flow-induced changes in the pore pressure as the liquid cap dries out and capillary effects leads to two distinct modes of air invasion. Monitoring the air-invasion-induced changes to the transmitted light intensity can serve as a convenient visual assessment of the pressure profile inside the deposit. Our predictive model accounting for the stresses inside drying films of colloidal suspensions can provide guidelines for exploiting crack formation in patterning applications[49,50] and for preventing thin-film failure in coating processes.[51]

ASSOCIATED CONTENT

Supporting Information

The Supporting Information is available free of charge at https://pubs.acs.org/doi/10.1021/acs.langmuir.2c00397.

Measurements of the deposit thickness profile for different particle volume fractions; visualizations of the liquid cap retraction and crack formation using a time-lapse reconstruction technique; measurements of the evaporation rate; derivation of the pressure profile $P(r)$ for different deposit widths; effect of the evaporative flux profile on the pressure profile and on the pressure for crack formation (PDF)

Video S1: Bottom-view video of the drop pictured in Figure 3a, showing the avalanche-like propagation of radial cracks and the air invasion process occurring before the liquid cap has disappeared. The elapsed time is 100 s. (MP4)

Video S2: Bottom-view video of the drop pictured in Figure 3b, showing the air invasion process occurring after the liquid cap has disappeared. The elapsed time is 95 s. (MP4)

AUTHOR INFORMATION

Corresponding Authors

Paul Lilin − *Department of Mechanical Engineering, Massachusetts Institute of Technology, Cambridge, Massachusetts 02139, United States;* orcid.org/0000-0002-5767-3551; Email: plilin@mit.edu

Irmgard Bischofberger − *Department of Mechanical Engineering, Massachusetts Institute of Technology, Cambridge, Massachusetts 02139, United States;* Email: irmgard@mit.edu

Complete contact information is available at: https://pubs.acs.org/10.1021/acs.langmuir.2c00397

Notes

The authors declare no competing financial interest.

ACKNOWLEDGMENTS

We thank P. Bourrianne for help designing the experimental setup, and we acknowledge support from the MIT Research Support Committee.

REFERENCES

(1) Giorgiutti-Dauphiné, F.; Pauchard, L. Painting Cracks: A Way to Investigate the Pictorial Matter. *J. Appl. Phys.* **2016**, *120*, 065107.

(2) Tang, C.-S.; Zhu, C.; Cheng, Q.; Zeng, H.; Xu, J.-J.; Tian, B.-G.; Shi, B. Desiccation Cracking of Soils: A Review of Investigation Approaches, Underlying Mechanisms, and Influencing Factors. *Earth-Sci. Rev.* **2021**, *216*, 103586.

(3) Brutin, D.; Sobac, B.; Loquet, B.; Sampol, J. Pattern Formation in Drying Drops of Blood. *J. Fluid Mech.* **2011**, *667*, 85−95.

(4) Hertaeg, M. J.; Tabor, R. F.; Routh, A. F.; Garnier, G. Pattern Formation in Drying Blood Drops. *Philos. Trans. R. Soc., A* **2021**, *379*, 20200391.

(5) Routh, A. F. Drying of Thin Colloidal Films. *Rep. Prog. Phys.* **2013**, *76*, 046603.

(6) Deegan, R. D.; Bakajin, O.; Dupont, T. F.; Huber, G.; Nagel, S. R.; Witten, T. A. Capillary Flow as the Cause of Ring Stains from Dried Liquid Drops. *Nature* **1997**, *389*, 827−829.

(7) Parisse, F.; Allain, C. Shape Changes of Colloidal Suspension Droplets during Drying. *J. Phys. II* **1996**, *6*, 1111−1119.

(8) Lee, S. Y.; Gradon, L.; Janeczko, S.; Iskandar, F.; Okuyama, K. Formation of Highly Ordered Nanostructures by Drying Micrometer Colloidal Droplets. *ACS Nano* **2010**, *4*, 4717−4724.

(9) Bourrianne, P.; Lilin, P.; Sintes, G.; Nirca, T.; McKinley, G. H.; Bischofberger, I. Crack Morphologies in Drying Suspension Drops. *Soft Matter* **2021**, *17*, 8832−8837.

(10) Lilin, P.; Bourrianne, P.; Sintès, G.; Bischofberger, I. Blooming Flowers from Drying Drops. *Phys. Rev. Fluids* **2020**, *5*, 110511.
(11) Allain, C.; Limat, L. Regular Patterns of Cracks Formed by Directional Drying of a Colloidal Suspension. *Phys. Rev. Lett.* **1995**, *74*, 2981−2984.
(12) Giorgiutti-Dauphiné, F.; Pauchard, L. Elapsed Time for Crack Formation during Drying. *Eur. Phys. J. E* **2014**, *37*, 39.
(13) Yan, N.; Luo, H.; Yu, H.; Liu, Y.; Jing, G. Drying Crack Patterns of Sessile Drops with Tuned Contact Line. *Colloids Surf., A* **2021**, *624*, 126780.
(14) Lee, W. P.; Routh, A. F. Why Do Drying Films Crack? *Langmuir* **2004**, *20*, 9885−9888.
(15) Sobac, B.; Colinet, P.; Pauchard, L. Influence of Bénard−Marangoni Instability on the Morphology of Drying Colloidal Films. *Soft Matter* **2019**, *15*, 2381−2390.
(16) Pauchard, L.; Parisse, F.; Allain, C. Influence of Salt Content on Crack Patterns Formed through Colloidal Suspension Desiccation. *Phys. Rev. E* **1999**, *59*, 3737−3740.
(17) van der Kooij, H. M.; van de Kerkhof, G. T.; Sprakel, J. A Mechanistic View of Drying Suspension Droplets. *Soft Matter* **2016**, *12*, 2858−2867.
(18) Ghosh, U. U.; Chakraborty, M.; Bhandari, A. B.; Chakraborty, S.; DasGupta, S. Effect of Surface Wettability on Crack Dynamics and Morphology of Colloidal Films. *Langmuir* **2015**, *31*, 6001−6010.
(19) Carle, F.; Brutin, D. How Surface Functional Groups Influence Fracturation in Nanofluid Droplet Dry-Outs. *Langmuir* **2013**, *29*, 9962−9966.
(20) Lama, H.; Gogoi, T.; Basavaraj, M. G.; Pauchard, L.; Satapathy, D. K. Synergy between the Crack Pattern and Substrate Elasticity in Colloidal Deposits. *Phys. Rev. E* **2021**, *103*, 032602.
(21) Deegan, R. D. Pattern Formation in Drying Drops. *Phys. Rev. E* **2000**, *61*, 475−485.
(22) Berteloot, G.; Hoang, A.; Daerr, A.; Kavehpour, H. P.; Lequeux, F.; Limat, L. Evaporation of a Sessile Droplet: Inside the Coffee Stain. *J. Colloid Interface Sci.* **2012**, *370*, 155−161.
(23) Salamanca, J. M.; Ciampi, E.; Faux, D. A.; Glover, P. M.; McDonald, P. J.; Routh, A. F.; Peters, A. C. I. A.; Satguru, R.; Keddie, J. L. Lateral Drying in Thick Films of Waterborne Colloidal Particles. *Langmuir* **2001**, *17*, 3202−3207.
(24) Kaplan, C. N.; Mahadevan, L. Evaporation-Driven Ring and Film Deposition from Colloidal Droplets. *J. Fluid Mech.* **2015**, *781*, R2.
(25) Goehring, L.; Clegg, W. J.; Routh, A. F. Solidification and Ordering during Directional Drying of a Colloidal Dispersion. *Langmuir* **2010**, *26*, 9269−9275.
(26) Sanyal, A.; Basu, S.; Chaudhuri, S. Agglomeration Front Dynamics: Drying in Sessile Nano-Particle Laden Droplets. *Chem. Eng. Sci.* **2015**, *123*, 164−169.
(27) Routh, A. F.; Russel, W. B. Horizontal Drying Fronts during Solvent Evaporation from Latex Films. *AIChE J.* **1998**, *44*, 2088−2098.
(28) Lei, H.; Payne, J. A.; McCormick, A. V.; Francis, L. F.; Gerberich, W. W.; Scriven, L. E. Stress Development in Drying Coatings. *J. Appl. Polym. Sci.* **2001**, *81*, 1000−1013.
(29) Man, W.; Russel, W. B. Direct Measurements of Critical Stresses and Cracking in Thin Films of Colloid Dispersions. *Phys. Rev. Lett.* **2008**, *100*, 198302.
(30) Tirumkudulu, M. S.; Russel, W. B. Cracking in Drying Latex Films. *Langmuir* **2005**, *21*, 4938−4948.
(31) Yow, H. N.; Goikoetxea, M.; Goehring, L.; Routh, A. F. Effect of Film Thickness and Particle Size on Cracking Stresses in Drying Latex Films. *J. Colloid Interface Sci.* **2010**, *352*, 542−548.
(32) Xu, Y.; German, G. K.; Mertz, A. F.; Dufresne, E. R. Imaging Stress and Strain in the Fracture of Drying Colloidal Films. *Soft Matter* **2013**, *9*, 3735−3740.
(33) Xu, L.; Davies, S.; Schofield, A. B.; Weitz, D. A. Dynamics of Drying in 3D Porous Media. *Phys. Rev. Lett.* **2008**, *101*, 094502.
(34) Hu, H.; Larson, R. G. Evaporation of a Sessile Droplet on a Substrate. *J. Phys. Chem. B* **2002**, *106*, 1334−1344.
(35) Lama, H.; Basavaraj, M. G.; Satapathy, D. K. Tailoring Crack Morphology in Coffee-Ring Deposits via Substrate Heating. *Soft Matter* **2017**, *13*, 5445−5452.
(36) Dufresne, E. R.; Corwin, E. I.; Greenblatt, N. A.; Ashmore, J.; Wang, D. Y.; Dinsmore, A. D.; Cheng, J. X.; Xie, X. S.; Hutchinson, J. W.; Weitz, D. A. Flow and Fracture in Drying Nanoparticle Suspensions. *Phys. Rev. Lett.* **2003**, *91*, 224501.
(37) Yang, B.; Sharp, J. S.; Smith, M. I. The Interplay of Crack Hopping, Delamination and Interface Failure in Drying Nanoparticle Films. *Sci. Rep.* **2016**, *6*, 32296.
(38) Cazabat, A.-M.; Guéna, G. Evaporation of Macroscopic Sessile Droplets. *Soft Matter* **2010**, *6*, 2591.
(39) Crank, J. *The Mathematics of Diffusion*; Clarendon Press, 1979.
(40) Brinker, C. J.; Scherer, G. W. *Sol-Gel Science: The Physics and Chemistry of Sol-Gel Processing*; Academic Press: New York, 1990.
(41) Singh, K. B.; Tirumkudulu, M. S. Cracking in Drying Colloidal Films. *Phys. Rev. Lett.* **2007**, *98*, 218302.
(42) Osman, A.; Goehring, L.; Stitt, H.; Shokri, N. Controlling the Drying-Induced Peeling of Colloidal Films. *Soft Matter* **2020**, *16*, 8345−8351.
(43) Lee, J. Perspectives and Design Considerations of Capillary-Driven Artificial Trees for Fast Dewatering Processes. *Sci. Rep.* **2021**, *11*, 8631.
(44) Chiu, R. C.; Garino, T. J.; Cima, M. J. Drying of Granular Ceramic Films: I, Effect of Processing Variables on Cracking Behavior. *J. Am. Ceram. Soc.* **1993**, *76*, 2257−2264.
(45) Goehring, L.; Clegg, W. J.; Routh, A. F. Plasticity and Fracture in Drying Colloidal Films. *Phys. Rev. Lett.* **2013**, *110*, 024301.
(46) Birk-Braun, N.; Yunus, K.; Rees, E. J.; Schabel, W.; Routh, A. F. Generation of Strength in a Drying Film: How Fracture Toughness Depends on Dispersion Properties. *Phys. Rev. E* **2017**, *95*, 022610.
(47) Russel, W. B.; Wu, N.; Man, W. Generalized Hertzian Model for the Deformation and Cracking of Colloidal Packings Saturated with Liquid. *Langmuir* **2008**, *24*, 1721−1730.
(48) White, L. R. Capillary Rise in Powders. *J. Colloid Interface Sci.* **1982**, *90*, 536−538.
(49) Han, W.; Li, B.; Lin, Z. Drying-Mediated Assembly of Colloidal Nanoparticles into Large-Scale Microchannels. *ACS Nano* **2013**, *7*, 6079−6085.
(50) Phillips, K. R.; Zhang, C. T.; Yang, T.; Kay, T.; Gao, C.; Brandt, S.; Liu, L.; Yang, H.; Li, Y.; Aizenberg, J.; Li, L. Fabrication of Photonic Microbricks via Crack Engineering of Colloidal Crystals. *Adv. Funct. Mater.* **2020**, *30*, 1908242.
(51) Kanai, T.; Sawada, T. New Route to Produce Dry Colloidal Crystals without Cracks. *Langmuir* **2009**, *25*, 13315−13317.

https://doi.org/10.1021/acs.langmuir.2c00397
Langmuir 2022, 38, 7442−7447